Robust local and nonlocal transport in the topological Kondo insulator SmB_6 in the presence of a high magnetic field

Sangram Biswas,[1] Ramya Nagarajan,[1] Suman Sarkar,[1] Kazi Rafsanjani Amin,[1] M. Ciomaga Hatnean,[2] S. Tewari,[3] G. Balakrishnan,[2] and Aveek Bid[1,*]

[1]*Department of Physics, Indian Institute of Science, Bangalore 560012, India*

[2]*Department of Physics, University of Warwick, Coventry CV4 7AL, United Kingdom*

[3]*Department of Physics and Astronomy, Clemson University, Clemson, South Carolina 29634, USA*

(Received 23 February 2015; published 3 August 2015)

SmB_6 has been predicted to be a Kondo topological insulator with topologically protected conducting surface states. We have studied quantitatively the electrical transport through surface states in high-quality single crystals of SmB_6. We observe a large nonlocal surface signal at temperatures lower than the bulk Kondo gap scale. Measurements and finite-element simulations allow us to distinguish unambiguously between the contributions from different transport channels. In contrast to general expectations, the electrical transport properties of the surface channels were found to be insensitive to high magnetic fields. We propose possible scenarios that might explain this unexpected finding. Local and nonlocal magnetoresistance measurements allowed us to identify possible signatures of helical spin states and strong interband scattering at the surface.

DOI: 10.1103/PhysRevB.92.085103 PACS number(s): 73.25.+i, 71.27.+a, 72.25.−b, 73.20.−r

I. INTRODUCTION

Topological insulators (TIs) are a new class of materials where gapped bulk states coexist with gapless surface states having a linear energy-momentum dispersion relation protected by time-reversal symmetry [1–4]. These surface states are the consequence of the closing of the bulk gap at an interface as a result of the change of the nontrivial topology of the Hilbert space spanned by the wave function describing the insulator to a trivial one at the boundary of the material. The large spin-orbit coupling of the bulk material implies that Dirac fermions at the interface have helical spin polarization—the spin degeneracy of the Dirac fermions is lifted and the spin becomes transversely locked to the crystal momentum [5]. This leads to interesting possibilities, chief among them being the existence of Majorana modes in a proximity-induced superconducting state [6]. This and the obvious possible applications in spintronics have led the search for new robust TI materials.

SmB_6 has recently been predicted to be a topological Kondo insulator (TKI) [7,8]. At temperatures below few tens of Kelvin, a bulk energy gap opens up in this material due to hybridization of the conducting electrons in the 5*d* band and the localized moments in the 4*f* band leading to the appearance of a Kondo insulator state. In electrical transport measurements, this shows up as a rapid increase in the measured resistance as the material is cooled down below about 40 K. The presence of the bulk gap in SmB_6 down to at least 2 K has also been seen through capacitance measurements [9] and point-contact spectroscopy [10]. Below 4 K, the resistance was seen to saturate which could not be explained by the standard theory of Kondo insulators. Recently, it has been proposed that this low-temperature saturation of the resistance can be due to the appearance of topologically protected surface states in the Kondo gap. The existence of this surface state has been confirmed through resistivity measurements [11–13], nonlocal transport [12,13], angle-resolved photoemission spectroscopy (ARPES) [14–16], and point-contact spectroscopy [10]. A recent magnetic torque measurement, on the other hand, revealed quantum oscillations characteristic of a three-dimensional Fermi surface [17]. An important implication of the existence of topologically protected surface states is the existence of spin-momentum locking on the surface [5]. The cleanest signatures of this phenomenon come from spin-resolved ARPES measurements—to date, there is no convincing demonstration of this for the case of SmB_6. An alternate way of addressing this issue is through local and nonlocal magnetotransport studies which can probe the existence of spin helical surface states [18–21].

II. LOCAL AND NONLOCAL TRANSPORT MEASUREMENTS IN ZERO MAGNETIC FIELD

We have studied in detail local and nonlocal magnetotransport on high-quality single-crystal samples of SmB_6. The samples were prepared by the floating zone technique using a high-power xenon arc lamp image furnace [22]. Electrical contacts were defined on the (110) surface by standard electron-beam lithography followed by Cr/Au deposition. Before lithography, the sample surface was cleaned using concentrated HCl and then mirror polished to get rid of any surface contaminants. Defining the contacts lithographically enabled us to determine precisely the distance between the electrical probes, which was essential for the analysis presented in this paper. Electrical measurements were done using many different contact configurations on two different samples to unambiguously probe the local and nonlocal transport in the system—in the rest of the paper, we primarily discuss the data obtained in the configuration (labeled configuration A) described in Fig. 1(a). The local current i^l (shown by the olive arrow) flows between contact probes 4 and 7 and at low temperatures is confined only to the top surface of the device. The nonlocal current i^{nl} (shown by the red arrows), on the other hand, flows from the top surface successively through the left

*aveek.bid@physics.iisc.ernet.in

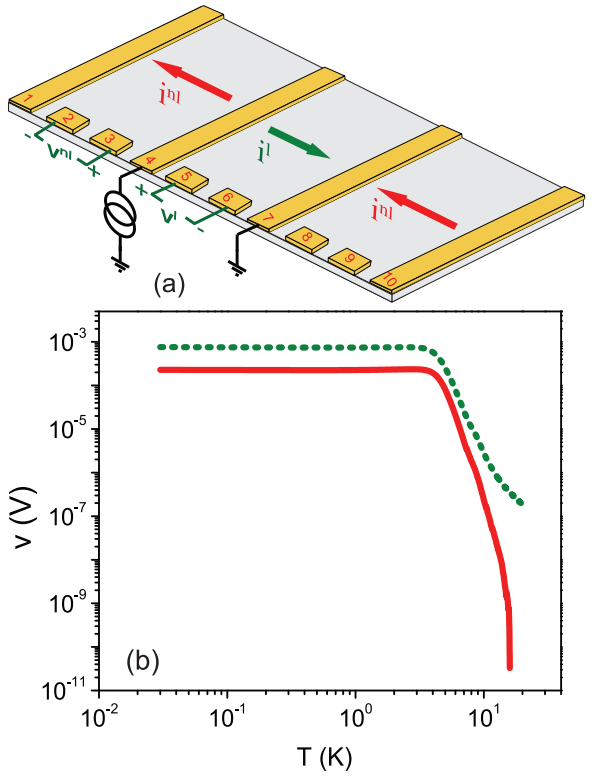

FIG. 1. (Color online) Local and nonlocal transport in SmB_6. (a) The figure shows the local and nonlocal measurement schemes for configuration A; arrows denote the direction of current flow. Contact pads numbered 1, 4, 7, and 10 were used as current and ground probes—these probes had dimensions $600 \times 100\,\mu m^2$. All other pads had dimensions $100 \times 100\,\mu m^2$ and were used as voltage probes. (b) v^l (olive dotted line) and v^{nl} (red solid line) measured in configuration A. The local voltage was measured between contact pads 5 and 6; 3 and 2 were used for nonlocal voltage measurements.

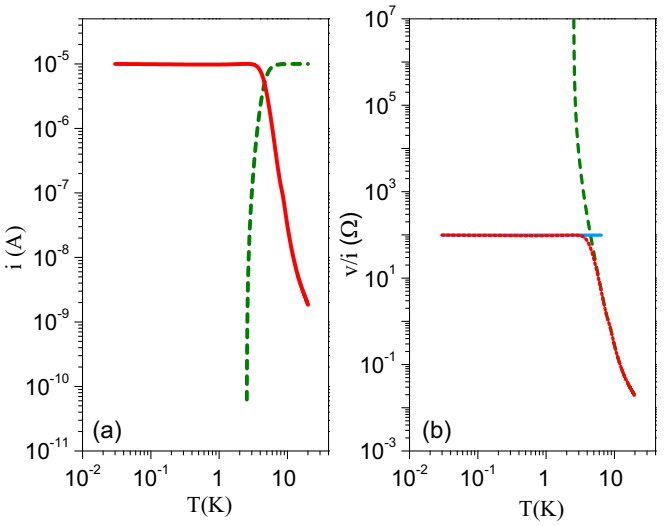

FIG. 2. (Color online) (a) Amount of current flowing through the bulk states (olive dotted line) and surface states (red solid line) as a function of temperature. (b) Green dashed line and cyan solid line show, respectively, the values of R_b and R_s as a function of temperature as extracted from our analysis; the red dotted line shows the experimentally measured v^l/i^l for the device.

side surface, bottom surface, right side surface, and back to the top surface before being collected at contact 7. Electrical measurements were performed using standard low-frequency ac measurement techniques by current biasing the sample in the temperature range 10 mK to 300 K and up to 16 T magnetic field. Figure 1(b) shows the measured local v^l and nonlocal v^{nl} voltages as a function of temperature measured at zero magnetic field. The local voltage v^l increases by five orders of magnitude as the device is cooled down from room temperature to below 1 K, attesting to the high quality of the sample. The value of the bulk band gap E_g extracted from v^l vs temperature measurements increased from 3.5 meV at 20 K to 5.5 meV at 9 K—this increase of the bulk Kondo gap with decreasing temperature is consistent with previous reports [10,23].

A significant nonlocal voltage v^{nl} appears below 15 K and increases rapidly by several orders of magnitude before saturating at temperatures below 3 K. The temperature at which the nonlocal signal appears corresponds to the energy scale of the many-body Kondo gap in this system. This appearance of the nonlocal signal concomitantly with the opening of the bulk Kondo gap strongly indicates that the two-dimensional surface conduction channels in SmB_6 emerge from the bulk topological Kondo insulator state and are not the result of accidental surface states (this was also verified by preparing the surface in different ways by varying the surface polishing method and duration of exposure to the ambient—the results were all quantitatively consistent with each other). The sharp increase in v^{nl} with decreasing temperature observed in our measurements can either be due to an increase in the resistance of the surface channel R_s or an increase in the fraction of total current flowing through the surface channel. As shown later in this paper, the resistance of the surface channel is almost independent of temperature and the increase in measured v^{nl} is because of an increase in surface current with decreasing temperature.

The total current driven through the sample gets distributed into three channels:

$$i_0 = i_b(T) + i_s^l(T) + i_s^{nl}(T). \tag{1}$$

Here, i_0 is the total applied current bias, $i_b(T)$ is the current flowing through the bulk of the sample, $i_s^l(T)$ is the local surface current, and $i_s^{nl}(T)$ is the nonlocal surface current. Equation (1) combined with the fact that the bulk resistance is activated down to the lowest temperature measured [9,10] allows us to extract the values of bulk and the surface current components over the entire temperature range (a more detailed discussion about this analysis has been presented in the Appendix). The results are plotted in Fig. 2(a). The results can be understood using the following argument: At high temperatures (above 15 K), current flows only through the bulk channel as the bulk resistance is very low in this temperature range. As the temperature decreases, the resistance of the bulk channel R_b diverges exponentially due to the opening up of the bulk energy gap. In comparison to R_b, the change in R_s is negligible over this temperature range. Consequently, the surface current increases rapidly with decreasing temperature and, at very low temperatures, almost the entire current flows

through the surface channels. The exact division of the surface current into the local $i_s^l(T)$ and the nonlocal $i_s^{nl}(T)$ components depends on the relative positions of the electrical contacts on the device and on the anisotropy of the sheet resistance tensor. Figure 2(b) shows a plot of R_s and R_b extracted from our analysis. Also plotted with a red dotted line is the measured v^l/i^l, which is a parallel combination of the resistances of the bulk channel and the local surface channel. The agreement of our calculated value with the experimental result supports the picture that R_s is almost constant throughout the temperature range below 15 K. However, a very small variation of R_s with temperature is found when the temperature in lowered below 3 K, which hints at richer physics underlying the surface states.

III. SIMULATIONS OF LOCAL AND NONLOCAL TRANSPORT

To get a quantitative understanding of the local and nonlocal surface transports in our device, we performed extensive simulations based on the finite-element method using COMSOL MULTIPHYSICS modeling software [24]. The model used is the Electric Currents, Shell (ecs) interface of the ac/dc module in COMSOL. This interface is used for modeling steady electric currents in thin current-conducting shells, following conservation of current and solving for the electric potential. The primary system of equations used in this module is

$$\vec{\nabla}.(t\mathbf{J}) = tQ_j, \tag{2}$$

$$\mathbf{J} = \sigma\mathbf{E} + \mathbf{J_e}, \tag{3}$$

$$\mathbf{E} = -\vec{\nabla}V, \tag{4}$$

where t is the thickness of the conducting shell, $\mathbf{J}$ is the current density, $\mathbf{J_e}$ is the externally generated current density, $\mathbf{E}$ is the electric field, σ is the electrical conductivity, and V is the potential. The model includes boundary conditions such as $\mathbf{J}\cdot\hat{n} = 0$ at various edges (material interfaces) and $V = V_0$ at specified boundaries.

In this study, the bulk resistance of the material was taken to be activated with the activation energy calculated from the experimentally measured resistance vs temperature plot at relatively high temperatures ($T > 5$ K). The surface conducting layer was modeled as a thin conducting shell of thickness t with a constant temperature-independent conductivity. The equations were solved for $J_e = 0$, $Q_j = 0$, $V = V_0$ at the current injecting probe and $V = 0$ at the ground. V_0 corresponds to the potential drop across the current probes for a 100 μA current injected into the system. The results of the simulations provided the potential distribution across the system from which the potential drops across the voltage probes were extracted. During the simulation, the surface conductivity was varied over a range of values until a good match (equivalent to a resistance 294$\Omega/\square$) with the experimental values was obtained. It was seen from the potential profiles obtained from the simulations that for certain measurement configurations, there was significant fringing of the equipotential curves fringe near the edges, resulting in a current flow through the side surfaces—an example is shown in Fig. 3. It was observed in such cases that the current flow

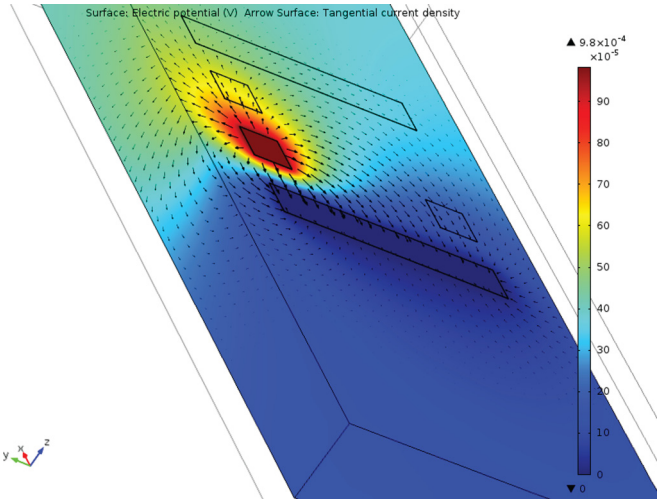

FIG. 3. (Color online) Electric-field profile obtained from our simulations for configuration 2NL (see Table I); the color bar in the images defines the potential profile in the surface. As we go far from source probe 9, the potential falls off. The arrows here show the direction of current flowing. Current in the nonlocal region does not stay only in the top surfaces, but they fringe and flow in the side surface and eventually in the bottom surfaces too.

through the xz surfaces was not uniform due to the fringing of the field, whereas the current through the yz surfaces was uniform with a constant current density.

The simulations were repeated for various shell thicknesses t in the range 1–200 Å, since the spatial distribution of the surface state has been reported to be around 10–20 Å [25]. The results are plotted in Fig. 4, where we show the extracted values of v^{nl} as a function of distance of the voltage probes from the source electrode—the result of the simulation was essentially independent of the shell thickness over this range of t values.

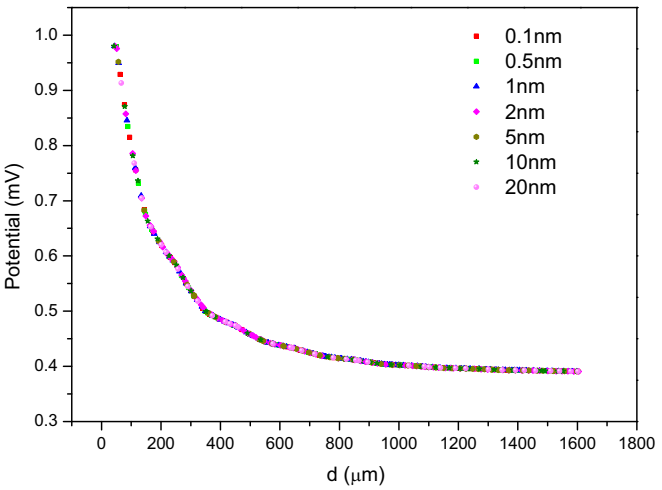

FIG. 4. (Color online) Calculated v^{nl} as a function of distance of the voltage probes from the source electrode; the numbers in the legend refer to the effective thickness of the conducting layer used for the simulations. It is seen that the various data sets collapse on top of each other.

TABLE I. Description of the electrical contact configurations used in this work; the numbers refer to the electrical probes as shown in Fig. 1(a). In the case of configurations 1NL and 2NL, the voltage probes were varied depending on the measurement.

Configuration	Source	Drain	Local V_+	Local V_-	Nonlocal V_+	Nonlocal V_-
A	4	7	5	6	3	2
C	1	4	2	3	6	5
E	7	10	8	9	6	5
1NL	2	1	variable	variable	variable	variable
2NL	9	10	variable	variable	variable	variable

All subsequent simulations were carried out on the system assuming a shell thickness $t = 1$ Å. The simulations were done for the various contact configurations mentioned in Table I. An example of the surface current densities and the electric-field profile obtained from the simulations for configuration A is shown in Fig. 5(a). The line profile of the electric potential on the surface was extracted from the simulations and is plotted in Fig. 5(b). The blue dashed line shows the potential profile on the top surface, while the red dotted line shows the potential profile for the bottom surface. Using this model, we calculated the dependence of the nonlocal surface potential at various distances from source contact d. The analysis of the nonlocal potential was complicated by the fringing of the electrostatic equipotential lines as one moves away from the source contact. To quantify the effect of this fringing on the nonlocal transport, we measured v^{nl} between equally spaced voltage probes located at different distances d from the source probe. Figure 5(c) shows the measured and calculated (from simulations) v^{nl} data. The excellent agreement between the measurement and simulation results lends credence to our model that transport in the ultralow-temperature range is through surface states only.

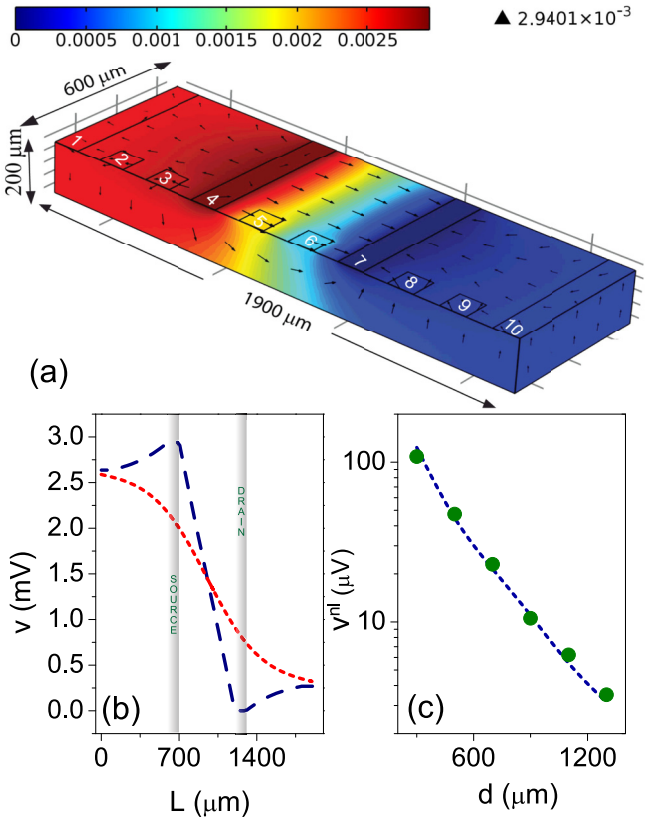

FIG. 5. (Color online) (a) Electric-field profile obtained from the finite-element simulations (see text for details). (b) Plot of the line profile of the electric potential on the top surface (blue dashed line) and bottom surface (red dotted line) extracted from the simulations as a function of the distance L from the left edge of the device. The shaded areas mark the position of the source and drain contact pads on the top surface. (c) Olive filled circles show the measured v^{nl} for voltage probes separated by 200 μm and located at an average distance d away from the current probe. The blue dashed line is obtained from the simulations for the same contact geometry.

IV. LOCAL AND NONLOCAL TRANSPORT IN FINITE MAGNETIC FIELD

To probe the effect of magnetic field on the surface states in SmB_6, we carried out local and nonlocal magnetotransport measurements in magnetic fields up to 16 T applied perpendicular to the plane of the device. If the system at low temperatures indeed goes into a topological Kondo insulator state, then conventional wisdom suggests that the surface states should quench in the presence of a magnetic field. Indeed, it has been shown in a previous work that the presence of magnetic impurities quenches the surface states in SmB_6 [11]. In Fig. 6(a), we plot the local magnetoresistance (MR) measured at 20 mK, while the nonlocal MR is plotted in Fig. 6(b). We find that in both cases, the magnetoresistance is positive until about 5 T and then it begins to fall. The local negative magnetoresistance seen at high magnetic fields has been reported before and occurs presumably due to suppression of the Kondo gap by the field [26,27]. The magnitudes of both the local and the nonlocal MR are very small—of the order of a few percentage even at 16 T magnetic field. This very small value of the MR is in contrast to what we expect for TI surface states in the presence of a time-reversal breaking field. On the other hand, it has been recently suggested [28–31] and experimentally demonstrated [32] that robust topologically protected spin helical states can indeed exist even under the conditions of broken time-reversal symmetry. This magnetic field insensitivity of topological surface states in two-dimensional topological insulators has been ascribed to a spin-Chern topological invariant. We note that the conduction through the surface states of time-reversal invariant topological insulators is also expected to be insensitive to time-reversal (TR) symmetry-breaking perturbations if the Fermi energy of the surface Dirac cones is not too close to the zero energy (which is where a gap is expected to open with TR breaking) and if the surface is relatively free of impurities.

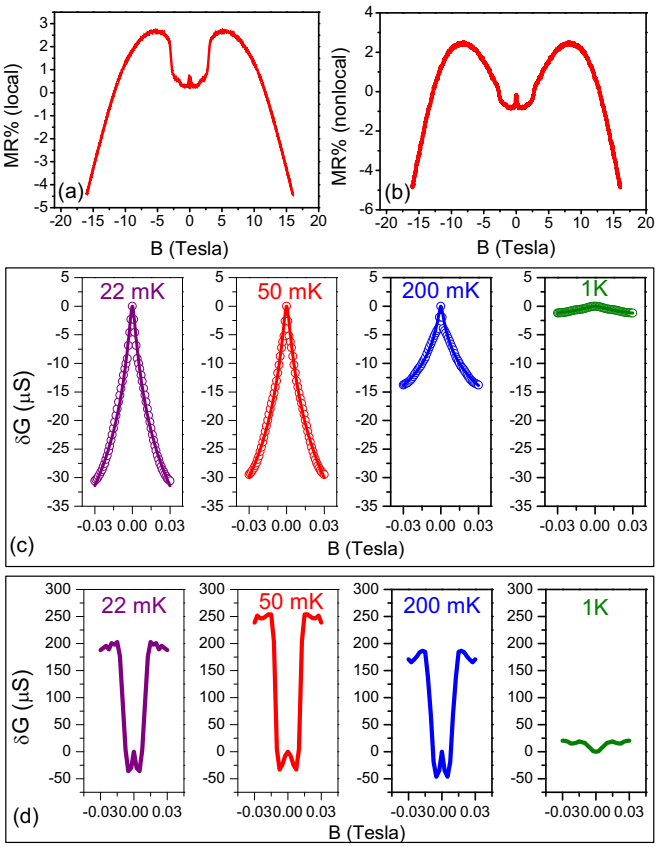

FIG. 6. (Color online) Magnetoresistance of the device. (a) Local MR measured in the range −16 to 16 T. (b) Nonlocal MR measured in the range −16 to 16 T. In both cases, the measurements were done at 20 mK. (c) Low-field local magnetoconductance (open circles) showing weak antilocalization at different temperatures. The solid lines are fits to Eq. (5). (d) Low-field nonlocal magnetoconductance as different temperatures.

From available angle-resolved photoelectron spectroscopy (ARPES) data [33,34], it can be seen that the energy difference between the Fermi energy for the surface states and the Dirac point is much higher than the Zeeman gap introduced in the spectrum due to the applied magnetic field. This might explain the apparent robustness of the surface states to the applied magnetic field. It has also been suggested that there can exist one-dimensional channels at the intersection of two surfaces of the three-dimensional topological insulators [35] or on the surface of the three-dimensional topological insulator due to potential variation on the surface [36,37]. These one-dimensional channels are predicted to exist even when the surface states get gapped out due to breaking of time-reversal symmetry. Another possibility is the existence of trivial surface states coexisting with topological surface states, in which case the MR signal would be a complicated convolution of the response of the topological surface states and trivial channels [38]. We believe that more experimental and theoretical work is needed to settle this issue.

The sharp peak near zero magnetic field in the local magnetoconductance, seen more clearly in the zoomed-in plot of magnetoconductance in Fig. 6(c), is due to the weak-antilocalization (WAL) effect, which is expected in the case of systems with large spin-orbit coupling [39]. The magnitude of this low-field positive MR decreases with increasing temperature, eventually vanishing above 2 K. This can be understood as follows: with increasing temperature, the inelastic-scattering rate of the charge carriers increases, which eventually destroys phase coherence of the conducting electrons essential for WAL [40,41]. The low-field local magnetoconductance $\sigma(B)$ at different temperatures was fitted to the Hikami-Larkin-Nagaoka (HLN) equation in the presence of large spin-orbit coupling [39]:

$$\sigma(B) - \sigma(0) = \alpha \frac{e^2}{2\pi^2 \hbar} \left\{ \ln\left[\frac{B_\phi}{B} - \psi\left(\frac{1}{2} + \frac{B_\phi}{B} \right) \right] \right\}, \quad (5)$$

where B_ϕ is related to the phase-coherence length l_ϕ as $B_\phi = \hbar/(4el_\phi^2)$. The fits yield $\alpha = 0.5$ in the temperature range 1 K > T > 0.1 K, which is the value expected for two-dimensional TI having a single coherent conducting channel. As the temperature decreases, the value of α steeply increases and saturates at temperatures below 50 mK to a value of about 1, which is the value expected for two independent topological coherent channels. Although this doubling of the parameter α with decreasing temperature has been reported recently in the case of the TI material Bi_2Te_3 [42], a proper understanding of this effect must await further theoretical investigations. In the absence of such detailed theoretical modeling, we conjecture that the saturation of the value of α to about 1 at the lowest temperatures indicates either the dominance of two surface Dirac bands from among the expected three bands or strong interband scattering, so that there are effectively only two conduction channels. The value of l_ϕ obtained from the fits to the low-field MR data was ≈700 nm at the lowest temperature. l_ϕ decreases with increasing temperature as a power law, $l_\phi \propto T^{-p/2}$ with $p \approx 1$, over the entire temperature range measured, suggesting that the major source of scattering is electron-electron interactions.

The low-field behavior of the nonlocal magnetoconductance, shown in Fig. 6(d), is not clear as it was in the case of local magnetoconductance. A possible reason could be that the local magnetotransport is confined only to the top surface of the device and hence is decided by the dispersion relation of only the [110] surface. The nonlocal current, on the other hand, flows through multiple (not only the top and bottom, but also the side) surfaces of differing crystallographic orientation and hence differing dispersion relations. This makes the low-field nonlocal MR very dependent on the exact electric and magnetic field profiles and hence quite difficult to tackle analytically. Understanding the nonlocal magnetotransport in these systems requires significant further investigations.

To conclude, we have studied the temperature and magnetic field dependencies of the local and nonlocal transport in the topological Kondo insulator SmB_6. In contrast to general expectations, the electrical transport properties of the surface channels were found to be insensitive to high magnetic fields. Local and nonlocal magnetoresistance measurements allowed us to identify signatures of transport through multiple Dirac bands, strong interband scattering at the surface, and possible indications of helical states in analogy with similar observations in Bi_2Se_3 [42]. Understanding the robustness of the surface states to magnetic fields requires further experimental and theoretical investigations.

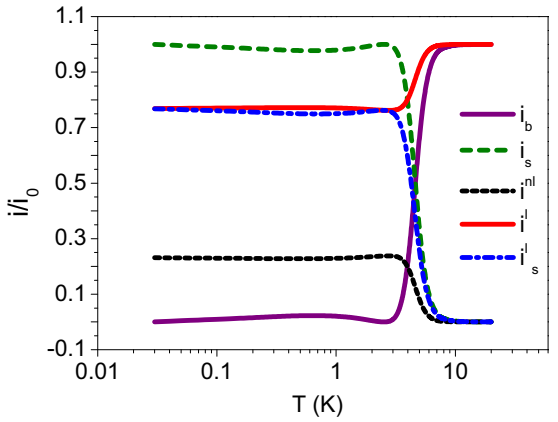

FIG. 7. (Color online) Different current components flowing through the device as a function of temperature. The values have been normalized by the bias current i_0.

ACKNOWLEDGMENTS

We acknowledge useful discussions with T. V. Ramakrishnan, Vijay Shenoy, Diptiman Sen, and Adhip Agarwala. A.B. acknowledges funding from Nanomission, Department of Science & Technology (DST) and Indian Institute of Science. The work at the University of Warwick was supported by EPSRC, UK (Grant No. EP/L014963/1).

APPENDIX: CALCULATION OF SURFACE AND BULK CURRENT COMPONENTS

At ultralow temperatures when the bulk conductance has frozen out, the applied current flows entirely through the surface, i.e., $i_s = i_0$. Then, we can write

$$V^l(T) = i_s^l(T)R_s(T);\ \ V^{nl}(T) = i_s^{nl}(T)R_s(T). \qquad \text{(A1)}$$

The amount of current flowing through the local and nonlocal regions depends on the effective resistances of the local and nonlocal channels, which in turn depend on the sample geometry and position of the probes. We can define a geometrical factor γ such that $i_s^l = \gamma i_s$. Using this along with Eq. (A1), we get $\gamma = (V^l)/(V^l + V^{nl})$ and $R_s = (V^l + V^{nl})/i_0$. From the measured values of v^{nl} and v^l we get $\gamma = 0.87$, 0.77, and 0.81 for configurations A, C, and E, respectively (see Table I). Assuming that the change in the surface resistance R_s with temperature is negligible in comparison to the orders of magnitude change in R_b, and using $i_s^{nl}(T) = V_{nl}(T)/R_s$, we get the values of the temperature-dependent nonlocal surface current. Subtracting this from the constant total current i_0 supplied to the sample gives the temperature-dependent local current $i^l(T)$ flowing through the sample. Subtracting the local surface current $i_s^l(T)[=V^l(T)/R_s]$ from the total local current $i^l(T)$ gives us bulk current $i_b(T)$. The values of the different current components obtained through this analysis are plotted in Fig. 7 as a function of temperature. It can be seen that at high temperatures, the entire current flows through the bulk of the device. At temperatures below 3 K, the current through the bulk of the device, i_b drops exponentially, and the entire current shifts to the surface channels. The nonlocal current i^{nl}, which was negligible until now, becomes a significant fraction (almost 20%) of the total current. The rest of the current flows through the local surface channel.

The geometry-dependent factor γ is decided by the effective resistances of the local and nonlocal transport channels,

$$\gamma = R^{nl}/(R^{nl} + R^l). \qquad \text{(A2)}$$

R^l depends only on the properties of the top surface as the local current flows only on the top surface. R^{nl}, on the other hand, depends on the properties of the top, bottom, and side surfaces. Assuming these surfaces have very similar specific resistances, we estimate $\gamma = 0.945$ for our device. Our experiments found the γ value to be almost 15% lower than this value. We believe this to be due to two reasons. First, our simulations show that there is a significant fringing of the electric-field lines. The second reason is that the transport in this material is anisotropic [43,44]. The local current is confined to a single-crystallographic surface and hence is not affected by any anisotropy in the system. The nonlocal current flows through two types of surfaces, i.e., the top and bottom surfaces form one type ($\langle 110 \rangle$ plane) of surface, while the two sides form the other type of surface. The combined path length of the top and bottom surfaces is 10.8 mm, while the combined path length of the two sides is 0.4 mm. Thus the ratio of the path lengths for the top+bottom surface to the two side surfaces is about 27:1. Hence the surface transport is predominantly determined by the conductivity of the top and bottom surfaces and the effect of any anisotropy in the resistivity between the different crystallographic directions is likely to be very small. Additionally, the results of the simulation are most relevant below about 7 K (when the surface conductance becomes comparable and eventually dominant over the bulk conductance) and, over this temperature range, the anisotropy in resistivity is small (see Fig. 1(a) in Phys. Rev. B **64**, 153103 (2001) and also Ref. [43]).

[1] M. Z. Hasan and C. L. Kane, Rev. Mod. Phys. **82**, 3045 (2010).
[2] J. E. Moore, Nature (London) **464**, 194 (2010).
[3] Y. Ando, J. Phys. Soc. Jpn. **82**, 102001 (2013).
[4] X.-L. Qi and S.-C. Zhang, Rev. Mod. Phys. **83**, 1057 (2011).
[5] C. L. Kane and E. J. Mele, Phys. Rev. Lett. **95**, 226801 (2005).
[6] L. Fu and C. L. Kane, Phys. Rev. Lett. **100**, 096407 (2008).
[7] M. Dzero, K. Sun, V. Galitski, and P. Coleman, Phys. Rev. Lett. **104**, 106408 (2010).
[8] F. Lu, J. Z. Zhao, H. Weng, Z. Fang, and X. Dai, Phys. Rev. Lett. **110**, 096401 (2013).
[9] D. J. Kim, T. Grant, and Z. Fisk, Phys. Rev. Lett. **109**, 096601 (2012).
[10] X. Zhang, N. P. Butch, P. Syers, S. Ziemak, R. L. Greene, and J. Paglione, Phys. Rev. X **3**, 011011 (2013).
[11] D.-J. Kim, J. Xia, and Z. Fisk, Nat. Mater. **13**, 466 (2014).
[12] D. J. Kim, S. Thomas, T. Grant, J. Botimer, Z. Fisk, and J. Xia, Sci. Rep. **3**, 3150 (2013).

[13] S. Wolgast, Ç. Kurdak, K. Sun, J. W. Allen, D.-J. Kim, and Z. Fisk, Phys. Rev. B **88**, 180405(R) (2013).
[14] J. Jiang, S. Li, T. Zhang, Z. Sun, F. Chen, Z. R. Ye, M. Xu, Q. Q. Ge, S. Y. Tan, X. H. Niu *et al.*, Nat. Commun. **4**, 3010 (2013).
[15] N. Xu, C. Matt, E. Pomjakushina, X. Shi, R. Dhaka, N. Plumb, M. Radović, P. Biswas, D. Evtushinsky, V. Zabolotnyy *et al.*, Phys. Rev. B **90**, 085148 (2014).
[16] N. Xu, P. K. Biswas, J. H. Dil, R. S. Dhaka, G. Landolt, S. Muff, C. E. Matt, X. Shi, N. C. Plumb, M. Radović *et al.*, Nat. Commun. **5**, 4566 (2014).
[17] B. S. Tan, Y.-T. Hsu, B. Zeng, M. C. Hatnean, N. Harrison, Z. Zhu, M. Hartstein, M. Kiourlappou, A. Srivastava, M. D. Johannes, T. P. Murphy, J.-H. Park, L. Balicas, G. G. Lonzarich, G. Balakrishnan, and S. E. Sebastian, Science **349**, 287 (2015).
[18] M. Liu, J. Zhang, C.-Z. Chang, Z. Zhang, X. Feng, K. Li, K. He, L.-l. Wang, X. Chen, X. Dai, Z. Fang, Q.-K. Xue, X. Ma, and Y. Wang, Phys. Rev. Lett. **108**, 036805 (2012).
[19] C. Shekhar, C. E. ViolBarbosa, B. Yan, S. Ouardi, W. Schnelle, G. H. Fecher, and C. Felser, Phys. Rev. B **90**, 165140 (2014).
[20] H.-T. He, G. Wang, T. Zhang, I.-K. Sou, G. K. L. Wong, J.-N. Wang, H.-Z. Lu, S.-Q. Shen, and F.-C. Zhang, Phys. Rev. Lett. **106**, 166805 (2011).
[21] S. Thomas, D. J. Kim, S. B. Chung, T. Grant, Z. Fisk, and J. Xia, arXiv:1307.4133.
[22] M. Ciomaga Hatnean, M. R. Lees, D. McK. Paul, and G. Balakrishnan, Sci. Rep. **3**, 3071 (2013).
[23] J. W. Allen, B. Batlogg, and P. Wachter, Phys. Rev. B **20**, 4807 (1979).
[24] http://www.comsol.com (unpublished).
[25] J. Lee, J.-H. Lee, J. Park, J. S. Kim, and H.-J. Lee, Phys. Rev. X **4**, 011039 (2014).
[26] A. Lacerda, D. Rickel, M. Hundley, P. Canfield, J. Thompson, Z. Fisk, P. Haen, and F. Lapierre, Phys. B: Condens. Matter **199**, 469 (1994).
[27] J. Cooley, C. Mielke, W. Hults, J. Goettee, M. Honold, R. Modler, A. Lacerda, D. Rickel, and J. Smith, J. Superconductivity **12**, 171 (1999).
[28] L. Sheng, D. N. Sheng, C. S. Ting, and F. D. M. Haldane, Phys. Rev. Lett. **95**, 136602 (2005).
[29] D. N. Sheng, Z. Y. Weng, L. Sheng, and F. D. M. Haldane, Phys. Rev. Lett. **97**, 036808 (2006).
[30] E. Prodan, Phys. Rev. B **80**, 125327 (2009).
[31] Y. Yang, Z. Xu, L. Sheng, B. Wang, D. Y. Xing, and D. N. Sheng, Phys. Rev. Lett. **107**, 066602 (2011).
[32] L. Du, I. Knez, G. Sullivan, and R.-R. Du, Phys. Rev. Lett. **114**, 096802 (2015).
[33] E. Frantzeskakis, N. de Jong, B. Zwartsenberg, Y. K. Huang, Y. Pan, X. Zhang, J. X. Zhang, F. X. Zhang, L. H. Bao, O. Tegus, A. Varykhalov, A. de Visser, and M. S. Golden, Phys. Rev. X **3**, 041024 (2013).
[34] M. Neupane, N. Alidoust, S.-Y. Xu, T. Kondo, Y. Ishida, D. J. Kim, C. Liu, I. Belopolski, Y. J. Jo, T.-R. Chang, H.-T. Jeng, T. Durakiewicz, L. Balicas, A. B. H. Lin, S. Shin, Z. Fisk, and M. Z. Hasan, Nat. Commun. **4**, 2991 (2013).
[35] O. Deb, A. Soori, and D. Sen, J. Phys. Condens. Matter **26**, 315009 (2014).
[36] R. Seshadri and D. Sen, Phys. Rev. B **89**, 235415 (2014).
[37] T. Yokoyama, A. V. Balatsky, and N. Nagaosa, Phys. Rev. Lett. **104**, 246806 (2010).
[38] Z.-H. Zhu, A. Nicolaou, G. Levy, N. P. Butch, P. Syers, X. F. Wang, J. Paglione, G. A. Sawatzky, I. S. Elfimov, and A. Damascelli, Phys. Rev. Lett. **111**, 216402 (2013).
[39] S. Hikami, A. I. Larkin, and Y. Nagaoka, Prog. Theor. Phys. **63**, 707 (1980).
[40] G. Bergmann, Phys. Rev. B **28**, 2914 (1983).
[41] F. Pierre, A. B. Gougam, A. Anthore, H. Pothier, D. Esteve, and N. O. Birge, Phys. Rev. B **68**, 085413 (2003).
[42] S.-P. Chiu and J.-J. Lin, Phys. Rev. B **87**, 035122 (2013).
[43] N. Sluchanko, V. Glushkov, S. Demishev, M. Kondrin, M. Ignatov, A. Pronin, A. Volkov, A. Savchenko, S. Kunii, V. Filippov *et al.*, Phys. B: Condens. Matter **312**, 331 (2002).
[44] V. Glushkov, N. Sluchanko, M. Ignatov, S. Demishev, S. Safonov, A. Savchenko, V. Fillipov, Y. Paderno, and S. Kunii, Acta Phys. Polon. B **34**, 1097 (2003).